Supporting Information

Guided Mode Resonance-Driven Photoluminescence Enhancement and Angular Emission Control in a 2-D Dielectric Photonic Lattice

Jagriti Ahuja[a], Saurabh Pandey[a], Shital Devinder[a], Jyoti Sardana[a], Anupriya Tiwari[a] , Nagarajan Subramaniyam [c], and Joby Joseph *[a,d,e]

[a.] *Photonics Research Lab, Physics Department, Indian Institute of Technology, Delhi, New Delhi, Delhi, 110016,*
[b.] *X-Fold Imaging Oy, FL-00076, Finland*
[c.] *Optics and Photonics Centre, Indian Institute of Technology Delhi, New Delhi, Delhi, 110016, India*
[d.] *Indian Institute of Technology Delhi– Abu Dhabi, Zayed City, Abu Dhabi, UAE*
E-mail: joby@iitd.ac.in

S1. Fabrication process flow for the TiO2-PET array

The nanoimprinted 2D periodic polyethylene terephthalate (PET) samples were manufactured by Xfold Imaging Oy, Finland. The fabrication process consists of two steps. First, the master mold was fabricated on a silicon substrate. The fabrication process to make the master mold begins with a thoroughly cleaned silicon substrate, treated using HF, solvents, SPM, or RCA methods, followed by oxygen plasma to enhance resist adhesion. A positive photoresist (AR-6200P) is spin-coated and soft-baked to remove solvent. Nanograting patterns are then defined using electron beam lithography (EBL) with a Vistec EPBG–5000pES system, supporting a wide range of feature sizes. The exposed resist is developed using AR 600-546, selectively removing the exposed areas. Subsequently, a reactive ion etching (RIE) step using Oxford Plasmalab 80Plus transfers the pattern into the substrate, producing anisotropic vertical profiles. Finally, the remaining resist is stripped using AR 600-71 and oxygen plasma cleaning. In the second step, nanoimprint lithography (NIL) was used. The NIL UV resist (mr-I-720R) was coated onto the PET plastic substrate using a spin-coating method followed by a soft bake. The master mold was then pressed against the resist-coated substrate, imprinting the pattern onto the resist. This step is performed using the nanoimprinting tool NPS300 from SUSS MicroTec. The imprinted 2D structures were cured via UV exposure. Before imprinting, the master mold was aligned to the correct position and plane relative to the PET substrate. The NIL process was conducted with optimized 0.3 MPa imprint pressure, with a stamp temperature of 130ºC. The imprinting time was maintained at 280s.

S2. Characterisation of dye film

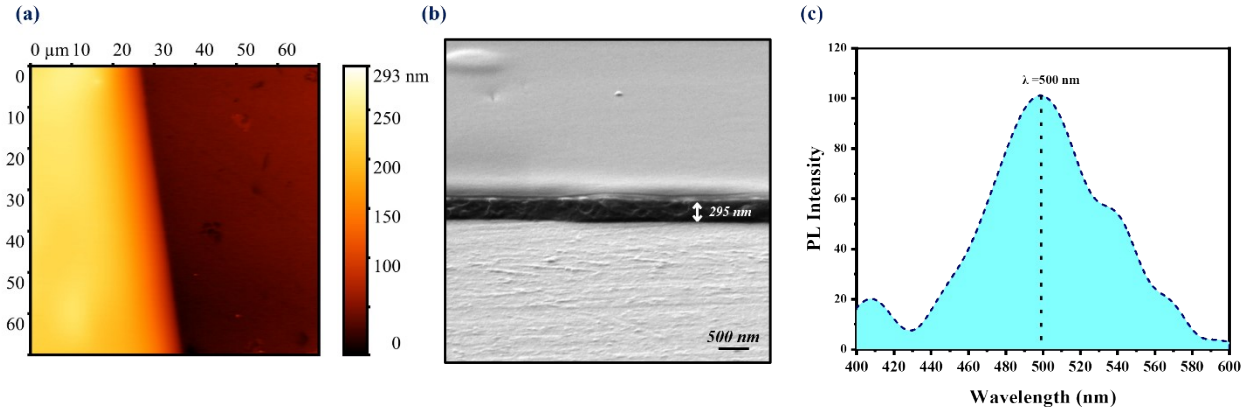

Figure S1. (a) AFM image of the Dye-PVA film (b) FESEM image of the Dye-PVA film spin-coated on the PET substrate. (c) Coumarin 481 emission spectrum when excited using a 405nm laser. Dye emission centered at 500 nm with a FWHM of ~ 80nm.

S3. Optical Transmission Setup

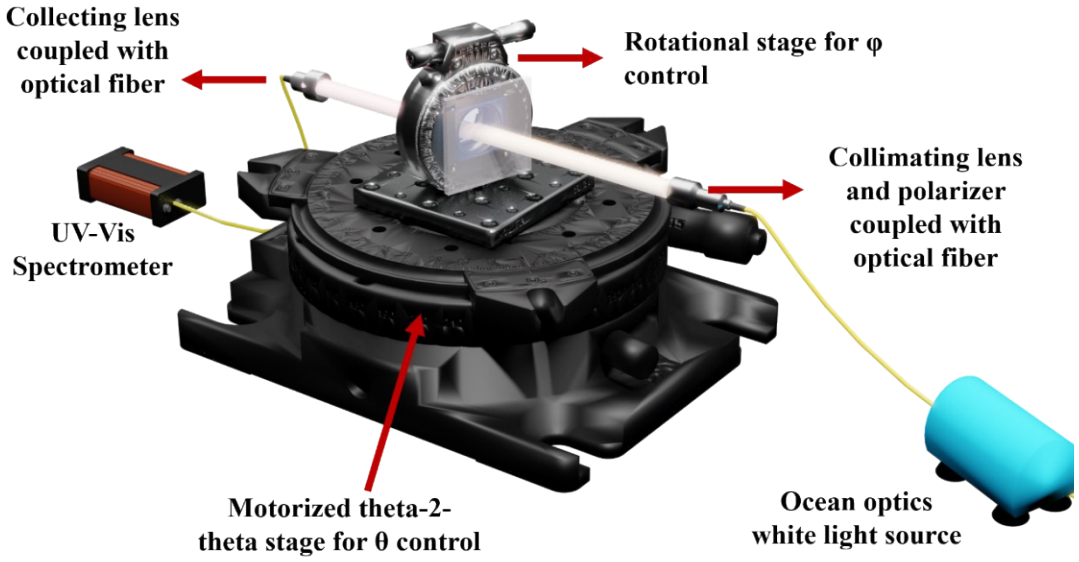

Figure S2. Optical setup for the measurement of the transmission/extinction spectrum. The sample is mounted on rotation stage and exposed to polarized broadband light (300-2000nm) from a halogen source (Ocean Optics flame). The transmitted light is collected through the spectrometer (Flame-S, Ocean Insight).

S4. Power-Dependent Photoluminescence and Photostability Measurements of Dye coated photonic array

To ensure the reliability of the PL measurements, the excitation power-dependent PL measurements for the photonic array with a 405 nm CW laser have been performed. The experimental setup for the

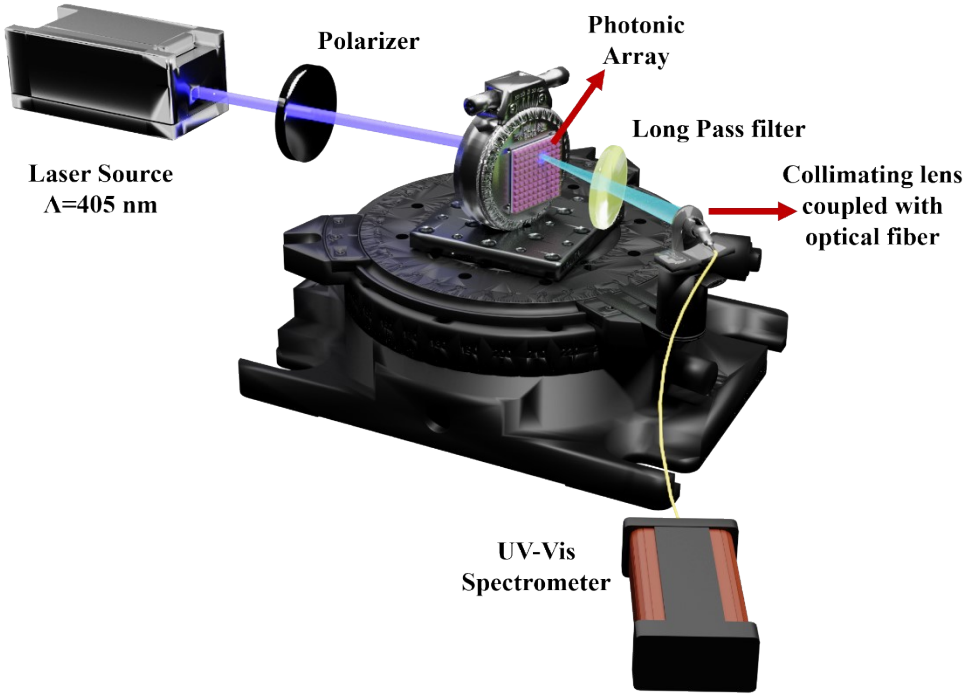

PL measurement is shown in Figure S3.

Figure S3. Experimental setup for measuring PL enhancement from the dielectric photonic array. The light is incident at a fixed angle, and the collection angle is varied by rotating the goniometer arm to capture the emitted light**.** A long-pass fluorescence filter is utilized to block the excitation light and transmit the PL emission only.

Figure S4 (a) shows the power-dependent PL curve of the dye-coated photonic array, where the PL intensity increases with excitation power. To evaluate the photostability of C481 dye, we have performed time-dependent PL measurements under continuous laser excitation. The results show a gradual decrease in PL intensity over time, characteristic of photobleaching, with the PL signal decreasing to approximately 20% of its initial value after 2000 seconds of continuous illumination at a fixed excitation power, as shown in Figure S4 (b). However, the decay is relatively moderate, after 30 minutes (1800 seconds), about **23.5%** of the original PL intensity remains.

Photobleaching, the irreversible loss of fluorescence under sustained excitation, can affect PL measurements, particularly at high excitation powers or with prolonged illumination. While the photostability curve indicates a moderate rate of photobleaching, it is important to emphasize that all

main PL measurements were acquired rapidly, with minimal exposure time for each sample. Each data

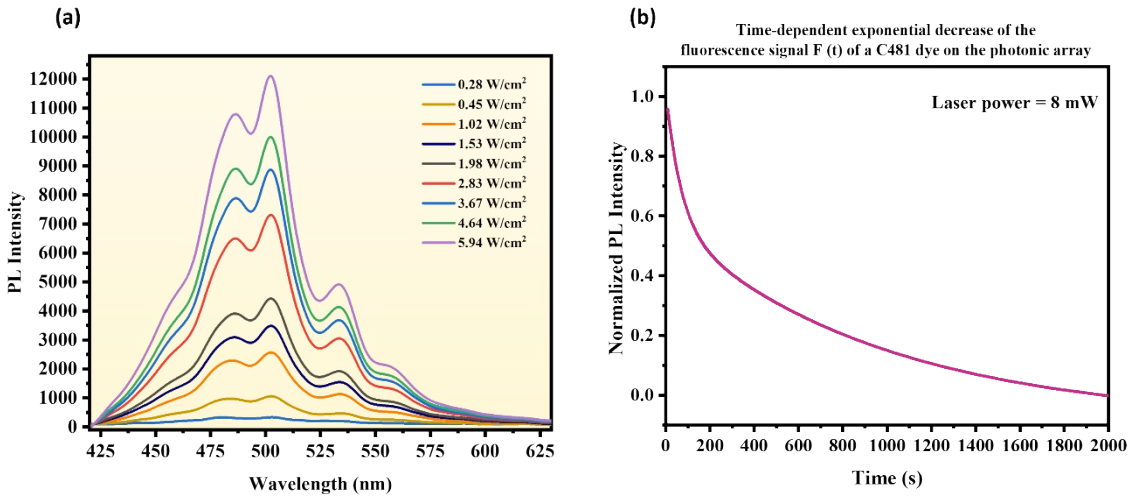

point was collected within a few seconds, well before significant photobleaching could occur and the dye emission remains stable over the measurement duration.

Figure S4. (a) Excitation power-dependent PL spectra of Coumarin 481 dye coated on the PET-TiO_2 photonic array showing consistent PL enhancement with increasing excitation intensity. (b) Normalized PL intensity as a function of continuous irradiation time with laser power = 8mW.

S5. Study of waveguide modes in TiO2-PET photonic lattice

For the PET-TiO_2 dielectric photonic array, two sharp GMR dips (Figure S4b) are observed in the experimentally obtained transmission spectra. We have done an extensive mode study to analyze the nature of the waveguide modes. The TE and TM polarizations of incident light satisfy different phase matching conditions for guiding at separate wavelengths. The effective refractive indices of TE and TM waveguide modes are calculated using the following equation[1]:

For TM waveguide mode: $$\tan(kt) = \frac{k(\gamma + \delta)}{k^2 - \gamma\delta} \quad (5.1)$$

For TE waveguide mode: $$\tan(kt) = \frac{n_w^2 k(n_s^2\gamma + \delta)}{n_s^2 k^2 - n_w^2\gamma\delta} \quad (5.2)$$

Effective refractive index of a waveguide mode: $$n_{eff} = \frac{\beta}{k_0} \quad (5.3)$$

Where $k = \sqrt{(n_w^2 k_0^2 - \beta^2}$, $\gamma = \sqrt{\beta^2 - n_s^2 k_0^2}$, $\delta = \sqrt{\beta^2 - k_0^2}$,

n_w, n_s denote the refractive indices of the waveguide and the substrate, respectively. k_0 is the free space wavenumber. β denotes the propagation constant of the waveguide. Utilizing the cross-sectional view of the TiO_2-PET structure depicted in the figure 1a (main text), where both TiO2 and PET have a thickness of 30 nm, we determined β for the transverse magnetic (TM) and transverse electric (TE) waveguide modes by numerically solving equations (1) and (2) respectively, It is determined that for the given thickness, only the TE0 and TM0 fundamental modes are supported, with effective mode indices of n^{TE0}=1.68871 and n^{TM0}=1.5901, respectively.[2]

The diffraction condition for a 2D lattice at normal incidence is governed by the following equation[3],

$$n_{eff} = \frac{\lambda_{diff} * \sqrt{m_1^2 + m_2^2}}{a}$$

(5.4)

Where λ_{diff} is the wavelength of the Bragg diffraction, and a is the periodicity of the lattice. The TE and TM diffraction wavelengths (dashed circles in Figure S5a) can be determined according to the diffraction orders and the effective refractive indices of the waveguide modes. The Waveguide GMR modes, as illustrated in Figure S5b, are the result of the coupling of the waveguide modes and diffraction orders[4].

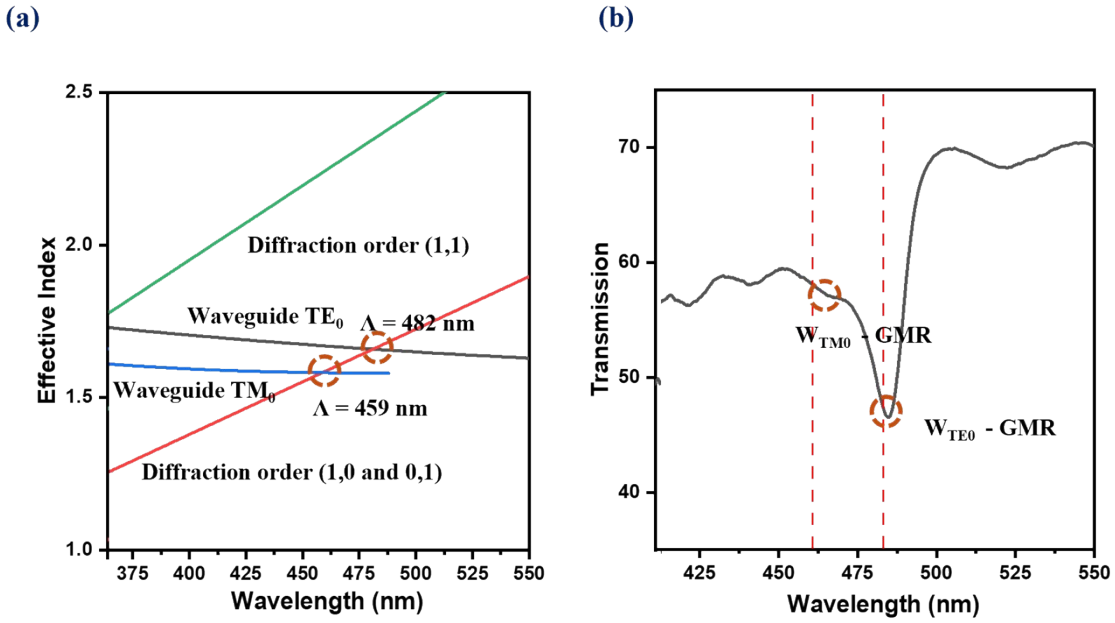

Figure S5. a) The diffraction conditions in the waveguide structure are dictated by the effective indices of the waveguide modes and the diffraction conditions of a periodic lattice with a periodicity of 300 nm. b) Optical transmission response of the PET-TiO_2 photonic array was experimentally observed,

highlighting the positions of GMR modes. The black curve represents the observed spectrum, with dips indicating the locations of TM0 and TE0 SLR excitations.

S6. Study of Optical band structure of the PET-TiO_2 photonic lattice.

At oblique incidence, the TE and TM waveguide modes can couple to diffracted from TE- and TM-polarized input light[5,6]. Figure S6(a(ii), b(ii)) illustrates the diffracted orders for a two-dimensional square periodic lattice diffracted by TE- and TM-polarized light.

The phase matching condition for a 2D square periodic structure, when a plane wave gets diffracted by it, is given by[7]:

$$\left(k_0\, sin\theta cos\emptyset + \frac{2\pi m}{a_x}\right)^2 + \left(k_0\, sin\theta sin\emptyset + \frac{2\pi m}{a_y}\right)^2 = \beta^2 \tag{6.1}$$

$$\left(k_0\, sin\theta + \frac{2\pi m}{a_x}\right)^2 + \left(\frac{2\pi m}{a_y}\right)^2 = (n_{eff}k_0)^2 \tag{6.2}$$

In the case of s-polarization (∅=0), the electric field aligns with the y-axis, while the projection of k_0 onto the xy-plane is aligned with the x-axis. The (m, n) = (±1,0) diffraction order of the lattice activates the TE_0 waveguide modes propagating in the ±x direction, resulting in a symmetrical splitting into two branches. The following equation governs these modes:

$$\pm k_0\, sin\theta + \frac{2\pi m}{a_x} = \pm\frac{2\pi}{\lambda} n_{eff}^{TE} \tag{6.3}$$

Simultaneously, the (m, n) = (0, ±1) diffraction orders can excite both TM_0 and TE_0 waveguide modes exhibiting conical diffraction, which show no splitting of the nearly flat dispersion curve and are governed by the following equation:

$$\sqrt{(k_0\, sin\theta)^2 + \left(\frac{2\pi m}{a_y}\right)^2} = \pm\frac{2\pi}{\lambda} n_{eff}^{TE/TM} \tag{4.4}$$

Conversely, for p-polarized light, the opposite occurs. Figure S6(e, f) represents the angular scan for the TiO_2-PET structure under TM and TE polarization of light. We have observed strong agreement between the experimental and the simulated dispersion diagrams for both polarizations. The normalized electric field profiles over the cross sections parallel and perpendicular to the incident electric field

vector are shown in Figures S6g and S6h, respectively, which confirms the TE and TM GMR modes at

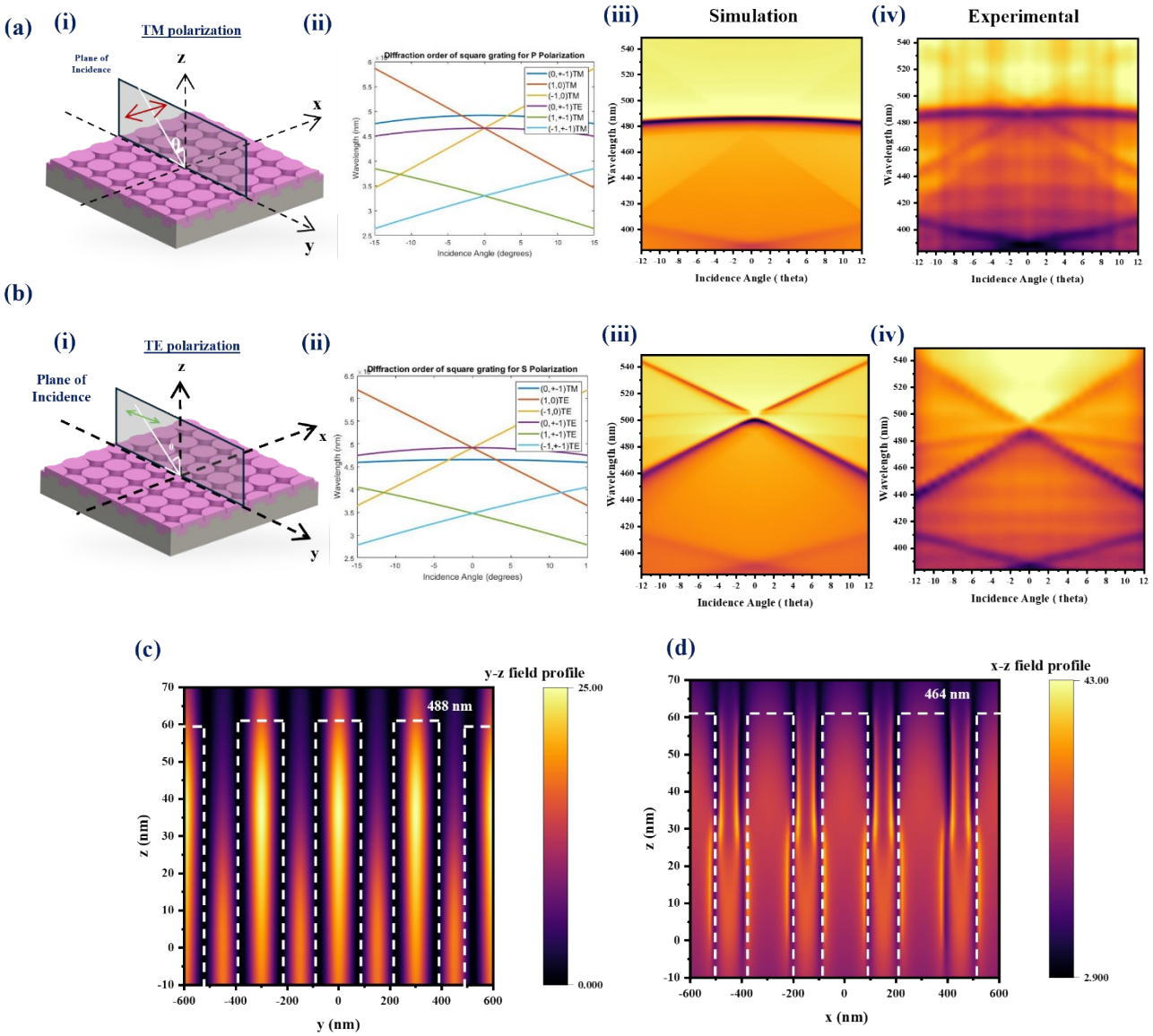

their 488 nm and 464 nm wavelengths, respectively.

Figure S6. (a) Angular exploration of resonant modes photonics under the influence of TM polarization. (i) schematic of the device under TM polarization (ii) Diffraction orders of a square periodic grating (iii) simulation and (iv) experimental angular dispersion curve b) Similar comparative studies under the effect of TE polarization. (c,d) Cross-section of normalized electric field distribution for GMR at λ = 488 nm and 464 nm.

S7. Study of waveguide modes in TiO_2-PET-Dye photonic lattice

The incorporation of a dye layer with a thickness of 300 nm on the TiO_2–PET dielectric array results in a redshift of the TE-GMR and TM-GMR to 515 nm and 491 nm, respectively. We have conducted the same analysis as in section S5 to reaffirm the characteristics of the dips found in the optical transmission curve. The incorporation of a refractive index layer of 1.56 and a thickness of 300 nm in the slab waveguide model facilitates the propagation of the TE0 and TM0 basic modes, yielding effective mode indices of n^{TE0}=1.76399 and n^{TM0}=1.6607, respectively. The TE and TM diffraction wavelengths (dashed circles in Fig. S7a) can be determined according to the diffraction orders equation (1.4) and the

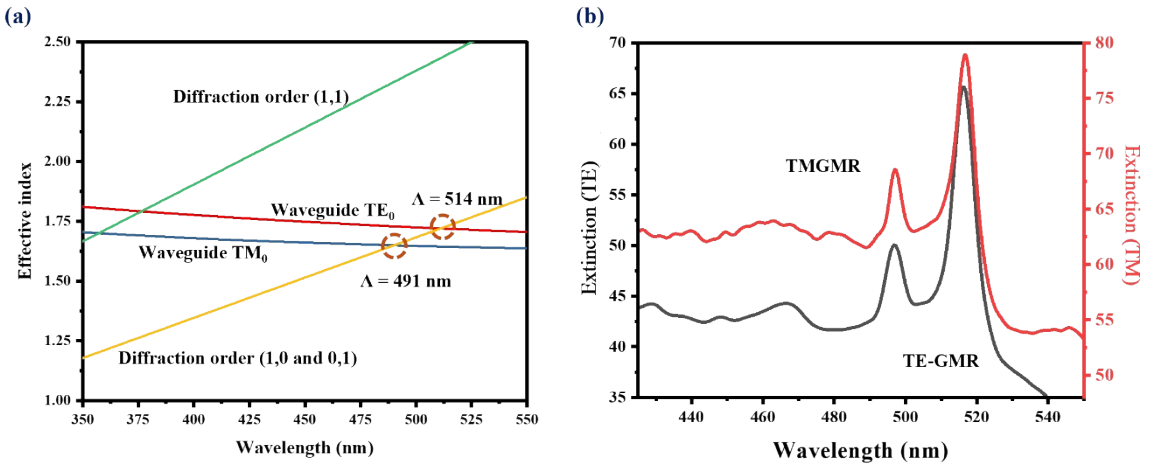

effective refractive indices of the waveguide modes.

Figure S7. a) The diffraction conditions in the waveguide structure are dictated by the effective indices of the waveguide modes and the diffraction conditions of a periodic lattice with a periodicity of 300 nm. b) Optical response of the PET-TiO_2 photonic array was experimentally observed, highlighting the positions of TM0 and TE0 GMR modes for TM and TE polarizations.

S8. Spatial and Orientational Dependence of the Purcell Factor

The Purcell factor quantifies the enhancement of the LDOS of an emitter due to its photonic environment, and its value is highly sensitive to the emitter's spatial position within a nanostructured array. We have performed a series of FDTD simulations[8], systematically mapping the relative LDOS as a function of dipole position along the x, y, and z axes within the unit cell, For the x-direction scans, the dipole source was placed at three representative heights: 50 nm (within the TiO_2 layer), 75 nm (at the top of the nanostructure), and 100 nm (inside the dye layer). This approach captures the spatial variation in LDOS both within and above the nanostructured array, as shown in Figure S8 (a–d). Owing to the structural symmetry, the results for the y direction are analogous to those for x.

The results depict that the LDOS enhancement peaks sharply near the GMR wavelength 515 nm and remains robust across lateral (x/y) positions at each height, but is highly sensitive to the vertical (z) placement of the emitter. The highest LDOS enhancement occurs when the emitter is in the region of strongest near-field confinement, specifically at or near the TiO_2 top surface, and the enhancement

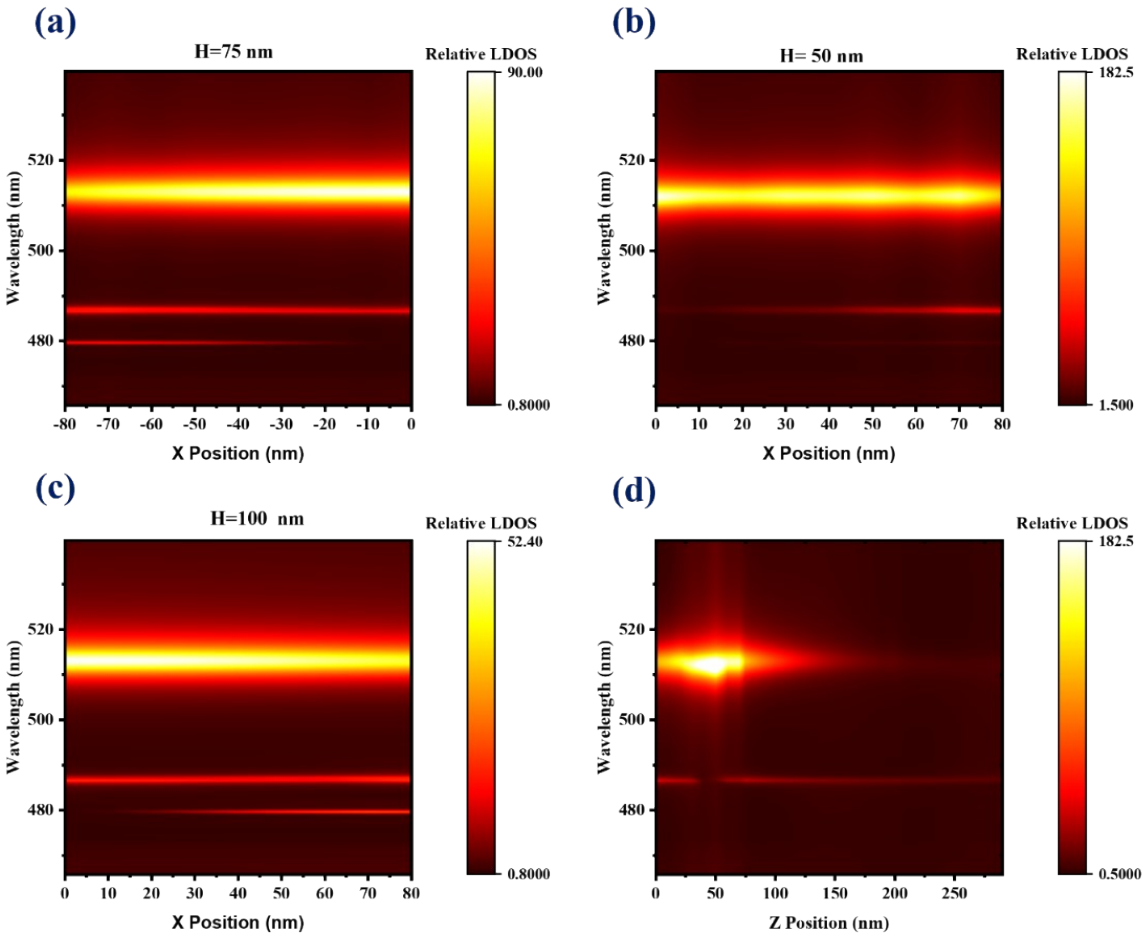

diminishes rapidly as the emitter is moved away from these regions.

Figure S8. Spatially resolved simulated maps of the relative LDOS for a dipole emitter placed at various positions within the photonic unit cell. LDOS as a function of lateral (x) position and wavelength at three different heights above the substrate: (a) 50 nm (within the TiO_2 layer), (b) 75 nm (at the top of the nanostructure), and (c) 100 nm (inside the dye layer). (d) LDOS as a function of vertical (z) position and wavelength.

To address the influence of dipole orientation on the relative LDOS in our dielectric photonic array, we systematically investigated how the simulated LDOS varies with the dipole angle ($\boldsymbol{\theta}$) relative to the array plane. As shown in Figure S9**,** when the dipole is positioned above the cavity and aligned normal

to the array plane **(**θ = 0°**),** the calculated relative LDOS remains close to unity, indicating that the spontaneous emission rate is nearly identical to that in free space. The overlap between the emitter dipole and the local electric field of the resonant mode is critical. When the dipole is oriented normal to the photonic array plane (θ=0), the relative LDOS remains minimal, close to unity, indicating weak coupling. This is because the emission is largely symmetric and does not efficiently interact with in-plane guided modes. As the orientation angle θ increases, the overlap with the in-plane electric field distribution of the guided-mode resonances (GMRs) improves. The maximum enhancement is observed when the dipole is oriented parallel to the array plane (θ=90), where the dipole efficiently excites the in-plane GMR modes, resulting in constructive interference and strong confinement of the emitted light within the photonic lattice. This angular dependence is consistent with both the theoretical framework and simulation results.

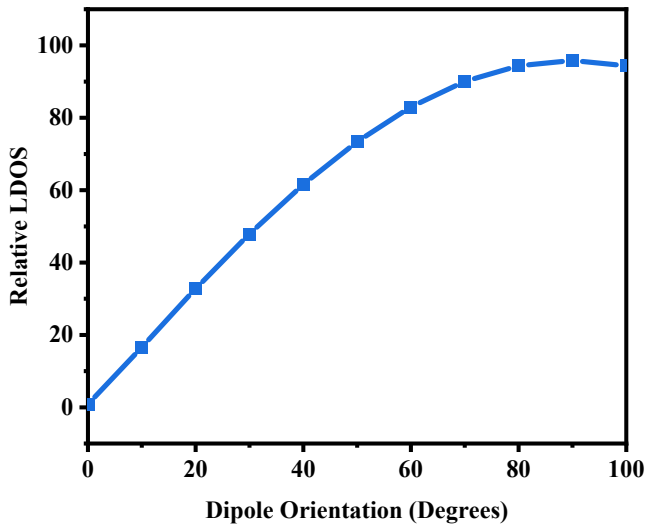

Figure S9. The dependence of the obtained relative LDOS on the orientation of the dipole emitter placed on top of the nano pillars.

S9. Purcell Factor Calculation Using the Mode Profile Formalism

For completeness, in addition to the LDOS-based approach described in the main manuscript, we have calculated the Purcell factor using the mode profile formalism as expressed in Equation 6 of the main manuscript:

$$F_p = \frac{3\,Q\,\lambda^3}{4\pi^2\,V_{eff}\,n^3}$$

The quality factor Q of the resonance was extracted from simulated spectral linewidths, which came around 85 at the resonance wavelength 515 nm. The effective mode volume is calculated using the standard expression[9,10]:

$$V_{eff} = \frac{\int \epsilon(\bar{r})|E(\bar{r})|^2 dV}{max[\epsilon(\bar{r})|E(\bar{r})|^2]}$$

where $\epsilon(r)$ is the local dielectric permittivity and $E(r)$ is the electric field profile of the GMR mode at the resonance wavelength (515 nm) was obtained from full-wave FDTD simulations. From the calculations V_{eff} of the mode came around 0.00185 μm^3. The approximated Purcell factor using this approach came around 120, which is consistent with the strong emission rate enhancement observed in both the experiment and LDOS-based simulations.

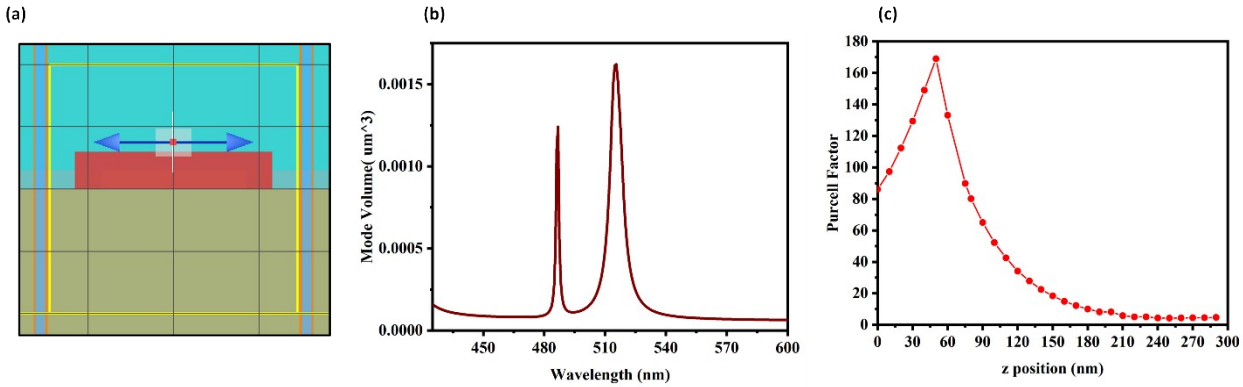

Figure S10. (a) Screenshot of the FDTD simulation region, showing the dipole source is placed at the top of the cavity (b). Mode volume vs wavelength plot obtained by simulating the cavity in periodic boundary conditions with a dipole source placed at the centre (c). Purcell Factor variation with z position of the emitter at the TE-GMR wavelength.

S10. Lifetime measurements of the Coumarin 481 dye with and without a photonic array.

To investigate the influence of near-field coupling on the emission decay rate from the dye-coated photonic array, Time-resolved PL (TRPL) measurements were performed and compared with a reference sample (dye coated on the PET substrate). The time-resolved (TR) fluorescence measurements in the nanosecond time domain were carried out using a time-correlated single photon counting (TCSPC) spectrometer from DeltaFlex, where samples were excited with a 375 nm diode laser (repetition rate 1 MHz, pulse width ~0.2ns) with laser power = 75 μW and fluorescence decays were

collected at right angle to the excitation pulses using a PPD detector. All the measurements were carried out with emission polarization set at a magic angle with respect to the vertically polarized excitation light beam, to eliminate the effect of reorientation of the dyes on the observed fluorescence decay.

The TRPL response is analyzed based on the carrier rate equation:

$$-\frac{dN}{dt} = AN + BN^2 + CN^3$$

where N is the photon-excited carrier density. The coefficients A and C correspond to the nonradiative Shockley-Reed-Hall recombination rate and the Auger recombination rate, respectively[11]. The coefficient B corresponds to the radiative recombination rate. Figure S11 shows the measured normalized PL emission decays from the dye-coated photonic array and the dye-coated PET substrate (reference sample). These decays are fitted with a tri-exponential function[12] to obtain the average lifetime of the decay. The average PL lifetime of dye molecules decreases from 3.37 ns for the reference sample to 0.15 ns for the photonic array at the GMR wavelength (515 nm). This marked reduction in lifetime provides direct experimental evidence of the Purcell effect, confirming a substantial enhancement in the spontaneous emission rate due to the photonic environment engineered by the array.

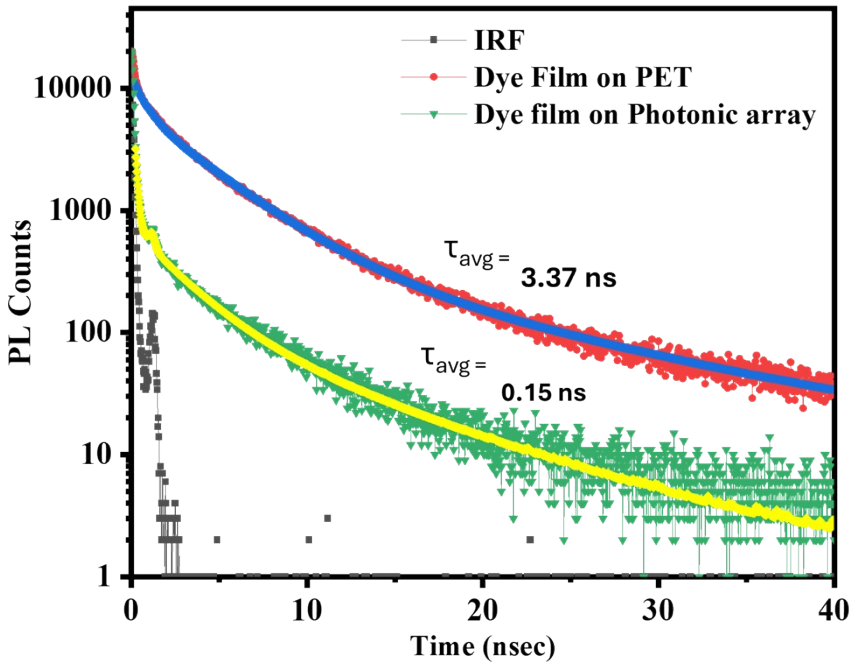

Figure S11. Lifetime measurements for the PVP-Dye film on PET substrate and on dielectric photonic array using a pulse laser at 375 nm.

S11. Analytical Model for the calculation of diffraction orders in the back focal plane image (BFP)

The excitation of lattice modes happens when the in-plane component of the incident plane wave's wavevector aligns with the wavevector of the lattice mode. This condition can be expressed mathematically as[13]:

$$n\frac{2\pi}{\lambda} = \sqrt{\left(\frac{2\pi}{\lambda} sin\theta\cos\emptyset + p\frac{2\pi}{P}\right)^2 + \left(\frac{2\pi}{\lambda} sin\theta\sin\emptyset + q\frac{2\pi}{P}\right)^2} \qquad (11.1)$$

where p and q are integers defining the diffraction orders, and n is the effective index. Solving the diffraction equation for the in-plane diffraction orders of the square periodic lattice allows us to determine the origin of the lines in the BFP image.

The periodicity of the designed array is 300 nm, and the emission wavelength is 515 nm, suggesting that diffraction orders are visible within the BFP image, as λ/P>1. This ensures that only the zeroth and first diffraction orders are visible within the back focal plane (BFP) image[14]. Figure S12 illustrates the solutions of Equation (11.1) with a periodicity of 300 nm for the wavelength of 515 nm, corresponding to the wavelength of the emitted light. The black solid lines denote the dispersion of the lattice modes (±1,0) with an effective index of 2.3 at the PET-TiO_2 interface, whereas the blue-dotted curve corresponds to the dispersion of the lattice modes (±1, ±1) with an effective index of 2.0 at the TiO_2-dye interface. The white dotted circle indicates the outer boundary of the BFP image captured by the collection optics, with a radius of (2π/λ) NA, where λ = 515 nm and NA = 0.75 represents the

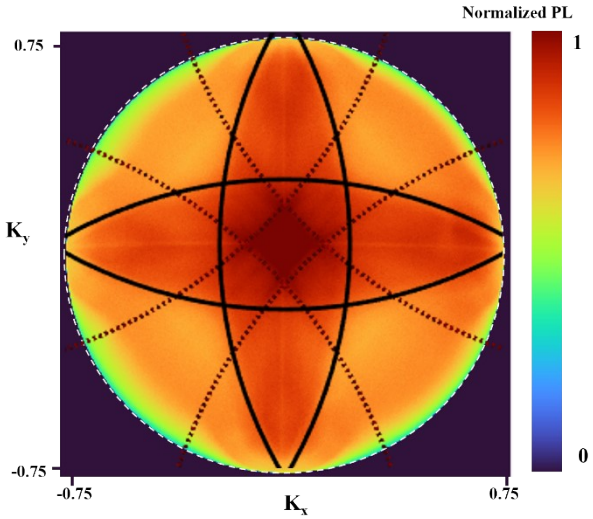

numerical aperture of the objective employed in BFP imaging.

Figure S12. Back focal plane (BFP) image representing photoluminescence (PL) emission at λ = 515 nm from the PET-TiO_2 photonic array covered with Coumarin 481 dye. The photonic array has a

periodicity of a = 300 nm. The blue dotted curves denote the (±1, ±1) in-plane diffraction orders at the TiO_2-dye interface, whereas the black solid curve signifies the (±1,0) in-plane diffraction orders at the PET-TiO_2 interface in momentum space.

S12. Quantitative Directional Emission Analysis

We have performed a systematic quantitative analysis of the angular emission characteristics using BFP images for both the dye-coated photonic array and the dye-coated glass sample to evaluate the directionality of the emission modes. Figure S13b presents the polar plot corresponding to the BFP image, comparing the emission profile of the photonic array (blue curve) with that of the same dye layer on an unstructured glass substrate (black curve) under identical measurement conditions. The angular confinement of the emission was quantified by calculating the FWHM of the main lobe. For the dye-coated photonic array, the FWHM was found to be approximately 20°, indicating a well-defined directional emission cone. In contrast, the unpatterned glass sample shows a much broader angular spread with an FWHM of **~90°**, confirming that the unstructured dye film emits isotropically.

To further quantify the quality of directional emission, the sidelobe suppression ratio (SSR) was evaluated[15,16]:

$$SSR(dB) = 10log_{10}\left(\frac{I_{\text{main peak}}}{I_{\text{max sidelobe}}}\right)$$

The extracted SSR for the photonic array was $\sim 2.83\ dB$, confirming effective suppression of side emissions and well-defined angular channels.

This quantitative BFP analysis confirms that the designed GMR structure provides robust and efficient directional emission with significant angular narrowing and sidelobe suppression compared to an unstructured control.

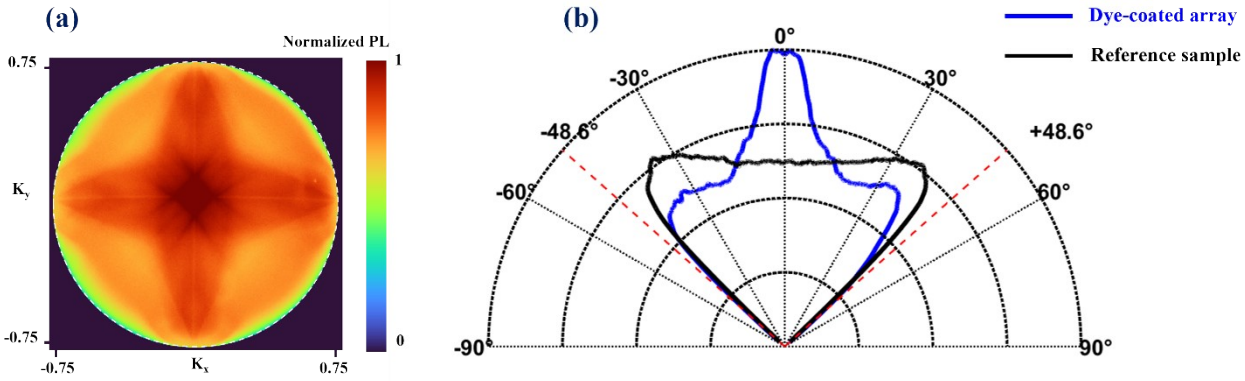

Figure S13. (a) Back focal plane (BFP) image of the PET-TiO_2 photonic array covered with Coumarin 481 dye. (b) Normalized PL enhancement as a function of zenith angle (theta) is obtained by cutting through the BFP at ky/k0 = 0. The blue curve is due to the dye-coated photonic array, and the black curve is due to the dye-coated glass sample. The red dashed lines refer to the maximum angle of emission that can be collected by the objective of NA=0.75.

S13. Comparative study on PL amplification

Structural Configuration	Emitting layer (PL wavelength)	Optical phenomena	PL Enhancement Factor	Directional Emission control	Purcell Factor	Year of publication
Chemically synthesized Ag metasurface[17]	organic layer: tris-(8-hydroxyquinoline) aluminum(Alq3) matrix doped with dichloromethane (DCM) emitters, $\lambda_{emission}$ = 620 nm)	Plasmonic	~20×	no	-	2022
TiO_2 frustum metasurfaces[18]	Nile red $\lambda_{emission}$ = 620 nm	Mie resonance	~10× at 620 nm	no	10	2021
Random plasmonic metasurfaces (Au, Al, Ag)[19]	Rhodamine 6G dye	LSPR	Varies by substrate, up to 200	no	Implied but not quantified	2022
Cylindrical Si rod arrays[20]	rhodamine 590 (R590)	Mie resonances and guided modes	1000	no	22	2018
Photonic crystal substrate by nanoreplica molding[21]	Cyanine-5 and cyanine-3	GMR	32× (Cy5), 25× (Cy3)	no	no	2010
2D periodic square hole arrays in SU-8 polymeric films coated with TiO_2 (high-refractive-	Organic dye-doped SU-8 layer	Optical resonances	Not specifically quantified	no	Yes (multiband lasing with controlled emission properties)	2025

index dielectric layer)[22]						
Nanoimprinted hexagonal arrays of aluminum nanoparticles[23]	Organic dye molecules	Lattice-induced hybrid plasmonic-photonic modes	4x	Yes (efficient beaming along narrow angular and spectral ranges)	12	2014
One-dimensional photonic crystal (PC) grating interfaces[24]	Fluorescent dye with emission maximum at 580 nm	GMR	>110-fold steering fluorescence enhancement	Yes (steering emission)		2024
silver nanostripes (~30nm thick) on silver film covered by PMMA layer[25]	R6G	**plasmonic bound states in the continuum**	5x	BFP imaging	Not explicitly quantified (Q-factors up to ~200)	2020
Hexagonal array of aluminum nanoparticle pyramids (475 nm lattice constant)[26]	Organic emitters (Lumogen F305, BASF)	Collective lattice resonances (SLRs) and quasiguided modes	Up to 24×		Not explicitly quantified	2013
Hexagonal array of ZrO_2 nanoparticles[27]	Coumarin 521T and $Eu(hfa)_3(TPPO)$	Both electric and magnetic Surface Lattice Resonances (SLRs)	~22× (electric SLR) and ~16× (magnetic SLR) with coumarin; ~16× for Eu transitions	Yes (angle-dependent)	No Purcell effect	2022
Stacked metasurfaces: TiO_2 nanoparticles (square lattice) and Al nanoparticles (hexagonal lattice)[28]	Lumogen F red 305 dye in PMMA	In-plane diffraction (TiO_2) and hybrid plasmonic-photonic modes (Al)	~15× for stacked metasurface	Yes (follows diffraction)	Small (10% lifetime decrease)	2021
Square arrays of gold nanodisks or dimers[29]	Single quantum emitter	Surface Lattice Resonances (SLRs)	13,803× (nanodisks array) 240,776× (gap antennas array)	Yes (beaming effect)		2017
Periodic array of PET-Tio2 pillars (This work)	Coumarin 481 dye	GMR	110-fold enhancement	Yes, Back focal plane imaging	100x	This Work
Chiral photonic	Ge- Vacancy	Symmetry	Not	Near-unity	5–20x	2023

crystals[30]	centers	breaking, spin–momentum locking	specifically quantified	directionality (>90%)		
Topologically engineered photonic platforms[31]	Quantum Dots	Topological edge states, spin–momentum locking	Not specifically quantified	High directionality	Up to 45x (inverse design)	2020

References

1 Y. Zheng and J.-A. Duan, *Optics and Photonics Journal*, 2011, **01**, 106–109.

2 Manfred Hammer, 1-D mode solver for dielectric multilayer slab waveguides , https://www.computational-photonics.eu/oms.html, (accessed 20 April 2025).

3 E. Sakat, G. Vincent, P. Ghenuche, N. Bardou, S. Collin, F. Pardo, J.-L. Pelouard and R. Haïdar, *Opt Lett*, 2011, **36**, 3054.

4 S. Sarkar, A. K. Ghosh, M. Adnan, O. Aftenieva, V. Gupta, A. Fery, J. Joseph and T. A. F. König, *Adv Opt Mater*, 2022, **10**, 2200954.

5 D. Wang, Q. Wang and Z. Zhan, *IEEE Photonics J*, 2018, **10**, 1–9.

6 S. Peng and G. M. Morris, *Opt Lett*, 1996, **21**, 549.

7 R. Amedalor, P. Karvinen, H. Pesonen, J. Turunen, T. Niemi and S. Bej, *Appl Phys Lett*, 2023, **122**, 161102.

8 Greens function and local density of states of a dipole source.

9 P. T. Kristensen, C. Van Vlack and S. Hughes, *Opt Lett*, 2012, **37**, 1649.

10 J. Ren, S. Franke, B. Vandrunen and S. Hughes, *Phys Rev A (Coll Park)*, 2024, **109**, 013513.

11 H. Kim, D. S. Shin, H. Y. Ryu and J. I. Shim, *Jpn J Appl Phys*, DOI:10.1143/JJAP.49.112402.

12 C. Chen, Y. Dou, J. Duan, H. Bie, J. Li, J. Yan and X. Wang, *Anal Chem*, 2025, **97**, 12276–12286.

13 D. Maystre, *Springer Series in Optical Sciences*, 2012, **167**, 39–83.

14 M. Born, E. Wolf, A. B. Bhatia, P. C. Clemmow, D. Gabor, A. R. Stokes, A. M. Taylor, P. A. Wayman and W. L. Wilcock, *Principles of Optics*, Cambridge University Press, 1999.

15 O. Shavit, H. Suaudeau, C. Julien, H. Klimovsky, N. Mañas-Chavernas, A. Salomon and M. Oheim, .

16 Q. Han, J. Shi and F. Shi, *Biomed Opt Express*, 2023, **14**, 1178–1191.

17 S. Hamdad, A. T. Diallo, M. Chakaroun and A. Boudrioua, *Sci Rep*, 2022, **12**, 3218.

18 Y. T. Lin, A. Hassanfiroozi, W. R. Jiang, M. Y. Liao, W. J. Lee and P. C. Wu, *Nanophotonics*, 2022, **11**, 2701–2709.

19 V. Anăstăsoaie, R. Tomescu, C. Kusko, I. Mihalache, A. Dinescu, C. Parvulescu, G. Craciun, S. Caramizoiu and D. Cristea, *Materials*, 2022, **15**, 1429.

20 M. Iwanaga, *Applied Sciences (Switzerland)*, 2018, **8**, 1328.

21 A. Pokhriyal, M. Lu, C. S. Huang, S. Schulz and B. T. Cunningham, *Appl Phys Lett*, 2010, **97**, 121108.

22 A. Conde-Rubio, J. R. Deop-Ruano, L. Cerdán, A. Manjavacas and A. Mihi, *Nanoscale Horiz*, 2025, **10**, 724–732.

23 G. Lozano, G. Grzela, M. A. Verschuuren, M. Ramezani and J. G. Rivas, *Nanoscale*, 2014, **6**, 9223–9229.

24 S. Bhaskar, W. Liu, J. Tibbs and B. T. Cunningham, *Appl Phys Lett*, 2024, **124**, 161102.

25 M. S. Bin-Alam, O. Reshef, Y. Mamchur, M. Z. Alam, G. Carlow, J. Upham, B. T. Sullivan, J.-M. Ménard, M. J. Huttunen, R. W. Boyd and K. Dolgaleva, DOI:10.1038/s41467-021-21196-2.

26 M. Ramezani, G. Lozano, M. A. Verschuuren and J. Gómez-Rivas, *Phys Rev B*, 2016, **94**, 125406.

27 M. Higashino, S. Murai, T. Y. Lo, S. Tomita and K. Tanaka, *J Mater Chem C Mater*, 2022, **10**, 9730–9739.

28 S. Murai, K. Agata and K. Tanaka, *J Appl Phys*.

29 F. Laux, N. Bonod and D. Gérard, *Journal of Physical Chemistry C*, 2017, **121**, 13280–13289.

30 H. Siampour, C. O'Rourke, A. J. Brash, M. N. Makhonin, R. Dost, D. J. Hallett, E. Clarke, P. K. Patil, M. S. Skolnick and A. M. Fox, *npj Quantum Inf*.

31 H. Siampour, O. Wang, V. A. Zenin, S. Boroviks, P. Siyushev, Y. Yang, V. A. Davydov, L. F. Kulikova, V. N. Agafonov, A. Kubanek, N. A. Mortensen, F. Jelezko and S. I. Bozhevolnyi, *Nanophotonics*, 2020, **9**, 953–962.